https://doi.org/10.5194/egusphere-2026-1638
Preprint. Discussion started: 11 May 2026

The North American CORDEX-CMIP6 WRF evaluation run: comparing historical simulations from 25 km to convection-permitting scales

Jacob Stuivenvolt-Allen[1], Trude Eidhammer[1], Rachel McCrary[1], Melissa Bukovsky[2], Stefan Rahimi[3], Hsin-I Chang[4], and Seth McGinnis[1]

[1]National Center for Atmospheric Research, Boulder, CO 80301
[2]Haub School of Environment and Natural Resources, University of Wyoming, Laramie, WY 82070
[3]Department of Atmospheric Science, University of Wyoming, Laramie, WY 82070
[4]Department of Hydrology and Atmospheric Science, University of Arizona, Tucson, AZ 85721

Correspondence: Jacob Stuivenvolt-Allen (jsallen@ucar.edu)

Abstract. Earth system models (ESMs) provide essential insight into large-scale climate variability and change but often lack the spatial resolution required to represent fine-scale processes critical for regional impacts and adaptation planning. To help address this gap, we present an updated high-resolution regional climate simulation for North America (NA) as part of the Coordinated Regional Downscaling Experiment (CORDEX). We evaluate a new reanalysis forced NA-CORDEX simulation at 12 km resolution against observational datasets, an earlier NA-CORDEX CMIP5 simulation (25 km), and the convection-permitting CONUS-404 simulation (4 km). Through these comparisons, we assess how horizontal resolution and regional model configuration influence historical biases and extremes, with a particular focus on precipitation processes given that convection is parameterized at 12 km. Relative to previous NA-CORDEX-CMIP5 simulations, the new CMIP6-based evaluation run reduces mean biases in temperature and precipitation, improves the magnitude and timing of the diurnal precipitation cycle across North America, and substantially improves the representation of tropical cyclone structure and intensity. Notably, extreme precipitation rates are well captured at 12 km when compared to the convection-permitting simulations. While long-term convection-permitting climate simulations remain a key objective for regional modeling, the current generation of CORDEX simulations provides a practical balance between computational efficiency and physical realism for continental-scale climate assessment.

1 Introduction

Regional climate simulations provide critical information for climate adaptation and decision-making by resolving atmospheric processes at scales finer than global Earth System Models (ESMs). The Coordinated Regional Downscaling Experiment (CORDEX) (Giorgi and Gutowski Jr, 2015) has facilitated the production of dynamically downscaled climate projections suitable for regional impact assessment. However, the fidelity of these projections depends critically on both model resolution and the representation of key physical processes.

https://doi.org/10.5194/egusphere-2026-1638
Preprint. Discussion started: 11 May 2026

A fundamental consideration in regional atmospheric modeling is the spatial resolution at which different processes can be explicitly resolved versus parameterized. For convection, 4 km resolution represents a critical threshold where this process can be permitted (Langhans et al., 2012). While convection-permitting simulations remain computationally prohibitive for ensembles of multi-decadal climate projections that adequately sample structural uncertainty over large domains (Qian et al., 2016), current-generation North American CORDEX (NA-CORDEX) simulations have progressed from 25–50 km in the CMIP5 era (Bukovsky and Mearns, 2020; Mearns et al., 2017) to 12 km horizontal resolution when driven by CMIP6 ESMs (Paquin et al., 2025). Although this resolution refinement enables better representation of topographic effects, land-surface heterogeneity, and mesoscale atmospheric features, it still requires parameterization of convective processes.

Recent advances in the Weather Research and Forecasting (WRF) model (Skamarock et al., 2019) include improvements to core physics schemes since the production of NA-CORDEX-CMIP5. The Noah Multi-Parameterization (Noah-MP) land surface model (Niu et al., 2011) offers advantages over the previous Noah land surface model (Tewari et al., 2004) through enhanced representation of vegetation dynamics, snow processes, and soil thermal and hydrological properties (He et al., 2023; Li et al., 2022). Multiple parameterization options in Noah-MP allow for more realistic simulation of land-atmosphere coupling and surface energy partitioning, which are critical for representing extremes in temperature and precipitation (Ma et al., 2017).

Similarly, the transition from the standard Rapid Radiative Transfer Model (RRTM) radiation scheme (Mlawer et al., 1997) to RRTMG (G stands for Global climate model) (Iacono et al., 2008) provides improved computational efficiency and more realistic treatment of aerosol and cloud radiative effects (Bae et al., 2016). The microphysics scheme has also evolved from the simpler WRF Single Moment 5 scheme (Hong et al., 2004) to the more sophisticated Thompson scheme (Thompson et al., 2008, 2016), which includes improved ice nucleation processes, graupel representation, and more realistic hydrometeor size distributions—all of which are essential for accurately simulating precipitation intensity and type.

Given the computational costs associated with convection-permitting simulations and the practical need for multi-decadal climate projections, we hypothesize that 12 km resolution represents a balance between physical realism and computational feasibility. However, evaluation is essential to understand which phenomena are well captured at this scale and where limitations persist. Here we present the model configuration and evaluation run of our contribution to NA-CORDEX, with two primary objectives: (1) assessing improvements from the corresponding previous-generation simulation and (2) identifying how these improvements compare to a similar simulation at convection-permitting scale.

To address these objectives, we compare climatological biases and meteorological phenomena between three WRF-based dynamically downscaled datasets: the 4 km convection-permitting CONUS404 (C404) dataset (Rasmussen et al., 2023), the new 12 km NA-CORDEX-CMIP6 (NAC6) simulation presented here, and the NA-CORDEX-CMIP5 (NAC5) simulation at 25 km (Mearns et al., 2017). The C404 and NAC6 simulations downscale the ERA5 reanalysis (Hersbach et al., 2020), while NAC5 downscales ERA-Interim (Balsamo et al., 2015). Although these simulations employ different physics configurations and spatial resolutions, they are otherwise very similar, and allow us to assess the quality of the new NAC6 simulations with minimal uncertainty due to structural differences between modeling systems.

https://doi.org/10.5194/egusphere-2026-1638
Preprint. Discussion started: 11 May 2026

2 Methods

2.1 WRF Configuration

2.2 Regional model configuration for NA-CORDEX-CMIP6

We use the WRF model version 4.6.1 with a domain that spans North America: it is 708 gridpoints east-to-west and 674 north-to-south, and centered on 97°W and 45°N (8496 km by 8088 km). There are 38 vertical levels and a model top of 50 hPa. The ERA5 reanalysis provides lateral boundary conditions, surface variables for initialization (soil moisture, skin temperature), sea surface temperature, and sea ice fraction. Land use and land-cover data is ingested from the United States Geological Survey (USGS). A relaxation layer of 10 gridpoints in each direction smooths the transition between the forcing data and the WRF simulation and is subsequently removed in post-processing. Spectral nudging of temperature, winds, and geopotential height is applied above the boundary layer for scales >1000 km to maintain synoptic consistency while resolving mesoscale processes.

We employ the physical parameterizations and configuration options listed in Table 1. These schemes were chosen through a blend of team and institutional experience with WRF and through systematic testing (Bukovsky and Karoly, 2009). In an effort to reduce climatological bias, we ran a suite of one-year tests for a 15-month period beginning in July of 1977. In these tests, one physics scheme was varied for up to four 15-month runs while the rest were held constant. For example, to choose a cumulus and convection scheme, we tested the following choices: the original Tiedtke (Tiedtke, 1989), an updated Tiedtke scheme which improved boundary-layer clouds (Zhang et al., 2011), the Kain-Fritsch cumulus potential scheme (Berg et al., 2013), and the Multi-Scale Kain-Fritsch scheme which employs a scale-dependent dynamic adjustment timescale (Zheng et al., 2016). The resulting test simulation with the smallest annual bias in temperature and precipitation was retained, and the next physics scheme was evaluated in subsequent tests.

The NAC6 ERA5 simulation is run in 12.4 year time-slices and initialized on August 11 of the starting year. The first two years and four months are discarded as spin-up, mostly to allow the land surface to equilibrate, and the next ten years are retained. In this case, January 1 of each new decade represents the beginning of a new time slice after spin up. Spectral nudging not only reduces general temperature and precipitation biases, but it also ensures clear continuity between these time slices. Running the model continuously would take impractical amounts of wallclock time (without queue times, it takes approximately 4 days of computational time to simulate a single year), especially when we downscale ESM data from 1950 through 2100.

2.3 CONUS404 and NA-CORDEX-CMIP5

The CONUS404 (C404) dataset comprises a 42-year (October 1979–September 2021) convection-permitting WRF Model version 3.9.1 simulation at 4-km resolution over the conterminous United States with 51 vertical levels extending to 50 hPa (Rasmussen et al., 2023). The physics configuration was optimized for convection-permitting simulations and includes custom land surface model modifications for improved snow cover representation. Initialized and integrated using ERA5 reanalysis boundary conditions, the model incorporates time-varying greenhouse gases, aerosol climatology, and prescribed ocean/lake

https://doi.org/10.5194/egusphere-2026-1638
Preprint. Discussion started: 11 May 2026

Table 1. Configuration comparison of WRF simulations across different model versions and resolutions.

Category		CONUS 404 (4 km)	NA-CORDEX-6 (12 km)	NA-CORDEX-5 (25 km)
Physics	Cumulus	—	New Kain-Fritsch	Old Kain-Fritsch
	Microphysics	Thompson & Eidhammer	Thompson	WSM-4
	Radiation	RRTMG	RRTMG	RRTM/CAM
	PBL	Yonsei University	Yonsei University	ETA Similarity
	Surface	MM5	MM5	MYJ
	Land Surface Model	Noah-MP	Noah-MP	Noah
Config	Vertical Levels	51	38	28
	Boundary	ERA5	ERA5	ERA-Interim
	Land Use	MODIS	USGS	USGS
	Forcings	GHG	GHG, Merra-AOD	GHG
	Urban Model	—	Single-level Canopy	—
	Lake Model	—	1-D Lake Model	—
	Nudging T/U/Z	Yes	Yes	Yes
	Nudging Q	No	No	Yes

temperatures (Hersbach et al., 2020; European Centre for Medium-Range Weather Forecasts, 2022). Spectral nudging of temperature, winds, and geopotential height is applied above the boundary layer for scales >1,800 km.

A disadvantage of using C404 for comparison is that it does not simulate much of Canada, Alaska, and Mexico. Much of our comparison and analysis is therefore focused on CONUS, even though the remit of NA-CORDEX is to simulate the entire continent. However, C404 is the only large-domain convection resolving historical simulation with WRF that has 30 years of overlap with both NAC5 and NAC6.

The NAC5 WRF simulations were run with WRF 3.5.1 (Mearns et al., 2017). The model is configured at 25 km horizontal resolution. Land surface processes are represented using USGS 24-category land use data, with boundary and initial conditions coming from ERA-Interim. Lateral boundary conditions are ingested from ERA-Interim Reanalysis with a linear relaxation over a relaxation zone of 10 gridpoints, with spectral nudging employed to maintain large-scale circulation consistency with driving data fields. Additional simulation details may be found in Diez-Sierra et al. (2022).

3 Results and Discussion

3.1 Climatological Biases

We begin by comparing climatological biases across the three historical WRF experiments from 1980 through 2010. Figure 2 displays mean temperature and precipitation biases relative to ERA5-Land data at 9 km horizontal resolution (Muñoz-Sabater

https://doi.org/10.5194/egusphere-2026-1638
Preprint. Discussion started: 11 May 2026

et al., 2021). The reanalysis data has been remapped to each WRF simulation resolution using conservative regridding, with biases calculated as simple differences between simulated and ERA5-Land values.

Temperature biases across all three simulations generally fall within ±3 °C, with notable reductions at higher resolutions. C404 and NAC6 exhibit remarkably similar spatial patterns of temperature bias, though the 12 km simulation shows slightly larger magnitudes. Rasmussen et al. (2023) suggest that throughout much of the western continent, which is characterized by high elevation and extreme topographic heterogeneity, there may be a resolution-dependent temperature bias in valleys smaller than the grid scale. Inadequate resolution of topography, land-surface features, and terrestrial water storage in sub-grid valleys could produce systematic warm biases, particularly for daily minimum temperatures (Barlage et al., 2021). This mechanism may contribute to the warm western bias present in both NAC6 and C404, which share the same Noah-MP land surface model. A key improvement from NAC5 to NAC6 is the substantial reduction of the cold bias throughout central and eastern North America.

Precipitation biases, shown in Figure 2d-f as percent differences from ERA5-Land climatological values, reveal distinct regional patterns. Both C404 and NAC6 show relatively dry conditions in lower elevation regions of the western US, with more balanced biases across higher elevations. The southeastern US exhibits a wet bias across all three simulations, though this bias is substantially larger in NAC5 and systematically reduced in both NAC6 and C404. Beyond CONUS, NAC6 displays a prominent wet bias throughout most of Mexico and western Canada. Overall, precipitation bias magnitudes decrease with increasing resolution when compared to NAC5. Precipitation biases are also presented in Figure S1 as differences in climatological precipitation rate (mm/day).

Recent work has suggested the eastern cold bias is likely related to snow hydrological conductivity parameterizations in Noah-MP (Zhang et al., 2025). Consistent with these findings, the annual biases in C404 and NAC6 appear to be primarily driven by larger seasonal biases during winter (Figure 3). Winter temperatures across all three datasets show systematic patterns: generally too warm across the western half of the continent and too cold in the east, especially at higher latitudes. NAC5 exhibits a much more extensive cold bias throughout central and eastern North America during winter, which is greatly reduced in both NAC6 and C404, apparently at the expense of a warmer western region. For brevity, we show only the winter and summer seasonal biases.

NAC6 exhibits a well known summertime warm bias throughout the plains (Liu et al., 2017), which provided motivation for major modifications to the shallow groundwater scheme in C404 (Barlage et al., 2021; Rasmussen et al., 2023). Coupled with this warm bias is a dry precipitation bias in JJA, which is still apparent in C404 (Figure 3b,d and Figure 4b,d) and other dynamically downscaled datasets using WRF (Rahimi et al., 2022; Liu et al., 2017). Precipitation biases are also presented in Figure S2 as differences in climatological precipitation rate (mm/day).

The western warm bias in NAC6 and C404 is mostly accounted for by biases in daily minimum temperatures (Figure S3). Daily maximum temperatures appear to be well simulated by C404 and NAC6, but daily minimum temperatures are consistently too warm by about 3-5°K throughout the western two-thirds of the continent. This bias is consistent with other high-resolution and convection-permitting simulations over the North America (Gensini et al., 2023).

https://doi.org/10.5194/egusphere-2026-1638
Preprint. Discussion started: 11 May 2026

3.2 Diurnal Processes

Convective warm season precipitation has proven challenging to simulate in ESMs and coarser resolution models (Gutowski Jr et al., 2020; Bukovsky and Karoly, 2011), especially diurnal precipitation processes linked to peak daytime heating (Kunkel et al., 2012; Geerts et al., 2017). We focus on three diurnal processes: (1) afternoon precipitation peaks in high-elevation regions of the Sierra Madre and Rocky Mountains, (2) eastward propagation of convection into the Great Plains and Upper Midwest, producing evening and nocturnal precipitation peaks (Trier et al., 2010; Dirmeyer et al., 2012), and (3) afternoon peaks in the Southeast US driven by maximum daytime heating (Scaff et al., 2020). Following Scaff et al. (2020), we estimate diurnal precipitation peaks by fitting a second-order harmonic function (Equation 1) to hourly precipitation from July 1 through August 31 for each year from 1980 through 2010, comparing the three WRF simulations against GPM IMERG V07B (Huffman et al., 2023). IMERG is preferred over ERA5-Land for evaluating sub-daily processes because ERA5-Land precipitation is simply interpolated from the coarser (31 km) ERA5 reanalysis grid to 9 km, meaning it does not resolve sub-grid convective structures any better than its parent product. Additionally, ERA5 precipitation is model-generated and subject to known biases in the phasing of convective precipitation (Dai, 2024), whereas IMERG captures observed diurnal cycle timing and amplitude, performing well against ground-based station estimates (Tan et al., 2019). ERA5-Land remains well suited for evaluating long-term climatological biases given its temporal coverage back to 1950.

$$P_t = P + A_1 \times cos(\frac{2\pi t}{24}) + B_1 \times sin(\frac{2\pi t}{24}) + A_2 \times cos(\frac{4\pi t}{12}) + B_2 \times sin(\frac{4\pi t}{12}) \quad (1)$$

Here P_t is precipitation at hour t, P is total daily precipitation, A_1 and B_1 control the 24-hour cycle, and A_2 and B_2 control the 12-hour cycle. Fourier transform estimates provide both the phase (hour of peak precipitation) and magnitude.

Figure 5a-d displays peak timing in local solar time (LST), while Figure 5e-h shows peak magnitude. IMERG (Figure 5a) clearly depicts afternoon peaks over the southern Rockies and Southeast US, plus propagation into the Great Plains. C404 captures both the precipitation spatial patterns and propagation well, with a slight underestimation of afternoon convective peaks in the southern Rockies. NAC6 reasonably captures the diurnal cycle with better peak timing in the Rockies. However, the peak timing over the NAM region along the Sierra Madre Occidental is mainly in the mid afternoon (fig.5c), slightly earlier than IMERG (fig. 5a). NAC6 also shows reduced propagation into the Great Plains and Upper Midwest—the dark blue shading representing nocturnal peaks does not extend as far eastward as in C404 and IMERG. Nevertheless, NAC6 substantially improves upon NAC5, which exhibits the homogeneous afternoon peak typical of ESMs and coarser RCMs (Lee and Wang, 2021).

IMERG excels at capturing diurnal precipitation cycles (Tan et al., 2019), though it under represents rainfall rates on timescales of 1 hour or less (Hosseini-Moghari and Tang, 2022), potentially explaining smaller magnitudes in Figure 5d-g compared to WRF simulations. All three WRF simulations show higher afternoon rainfall rates in the Southern Rockies, likely related to the North American Monsoon driving orographic precipitation (Boos and Pascale, 2021; Li et al., 2008). Beyond the Southern Rockies, coarser resolution datasets overestimate diurnal precipitation magnitude, particularly in the Southeastern US, consistent with Scaff et al. (2020).

https://doi.org/10.5194/egusphere-2026-1638
Preprint. Discussion started: 11 May 2026

Figure 6 shows a longitude-time Hovmöller diagram (latitudinally averaged from 35°-37°N) of mean JJA hourly precipitation, revealing afternoon peaks at 105°W beginning around 2:00 pm LST in all datasets. However, eastward convective propagation comparable to observations appears only in C404, though even this convection-permitting simulation underestimates the magnitude. While NAC6 improves upon NAC5 (consistent with Figure 5), both CORDEX simulations underestimate the longitudinal extent and magnitude of propagating convection originating at the Rockies.

Regional and global modeling experiments have generally underestimated the diurnal temperature range over land Mearns et al. (1995); Wang and Clow (2020), with variability across models likely depending on parameterizations of clouds, aerosols, land surface characteristics, and land-atmosphere interactions Lindvall and Svensson (2015); Mahony et al. (2022); Holt et al. (2006); Jach et al. (2022). While the numerous coupled sources of bias are difficult to disentangle, this problem provides an opportunity to compare each model's efficacy in simulating the diurnal temperature range (DTR; daily maximum minus minimum temperature).

We analyze mean spring (March through May) DTR, a period characterized by large differences in daily minimum and maximum temperatures. For C404 and NAC6, DTR is not homogeneously underestimated; both models overestimate daily temperature range compared to ERA5-Land in the Midwest, Great Lakes, and Pacific Northwest (Figure 7). NAC6 generally overestimates DTR more than C404 and NAC5, particularly across a wide swath of Canada directly overlapping with the evergreen needleleaf forest vegetation type (Figure 1b). Maximum daily temperatures have relatively small biases in this region (Figure S3), so the DTR bias stems primarily from minimum temperatures that are too cold. This suggests a structural bias in surface fluxes associated with this vegetation type in Noah-MP, possibly related to parameterized canopy-to-surface heat fluxes. Additionally, Zhang et al. (2025) show that the cold bias in eastern North America is strongly related to snow thermal conductivity parameters; increasing this parameter allows more heat exchange between the atmosphere and snowpack, raising winter temperatures substantially (up to 4°C) in the Northeast. Further analysis is needed to isolate the main sources of these temperature biases.

3.3 Seasonal Hydroclimate

Analysis of precipitation biases and the diurnal cycle of precipitation have suggested that the North American Monsoon in these WRF simulations is wet biased in the southwest US (Figures 4,5), and Figure 8 confirms this. In northern Mexico, the seasonal evolution of the monsoon in all three historical simulations matches IMERG quite well. Notably, the NAC6 run has the largest wet bias, though the magnitude of the simulated difference is quite small (approximately 0.5 mm/day).

In contrast, for the northern extent of the monsoon region in the southern US (Figure 8b), there is much more divergence in the simulated monsoon precipitation across the WRF simulations. All simulations are wet biased in the cold season (November through April), and then begin to diverge in Spring (April through June) at which point C404 most closely matches observations. The NAC6 run is the best at capturing the timing of the monsoon precipitation peak in August. Based on the summertime diurnal precipitation peaks and this climatological analysis, NAC6 has generally improved the seasonality and magnitude of the North American Monsoon compared to NAC5.

https://doi.org/10.5194/egusphere-2026-1638
Preprint. Discussion started: 11 May 2026

Another benefit of higher resolution is the improved representation of snow-relevant orographic processes, including terrain-induced circulation features and local ridge shadowing that reduces snow melt and sublimation (Rasmussen et al., 2011; McCrary et al., 2022; Ikeda et al., 2010). The land-surface model also plays a large role in the representation of snow and frozen water storage, which has been substantially improved in Noah-MP (used in NCA6 and CONUS404) by updates to radiative transfer and snow compaction (Abolafia-Rosenzweig et al., 2024; Lin et al., 2025).

We present an assessment of snow biases across the three WRF simulations, comparing against the University of Arizona SWE dataset (Broxton et al., 2019). We first look at the gridded biases of snow water equivalent (SWE) for the late winter and early spring (JFMAM) in the Western US (Figure 9). Spatial maps of climatological bias in SWE are displayed in the left column (Figure 9a,c,e) and distributions of the gridpoint-wise bias in elevation bands in the right column (b,d,f). From both the spatial maps and the distributions, a dry bias is evident in all simulations but it is noticeably smaller in the NAC6 and C404 simulations.

When comparing the gridded WRF data with station data, such as the SNOTEL sites analyzed in Figure 10, we expect WRF SWE to be lower than the SNOTEL sites because the gridpoint values represent an integration over a large area. The comparison with SNOTEL SWE are useful for providing an assessment of how well the WRF simulations capture the seasonality of the snow cycle, including the accumulation, peak, and melt phases.

We also compare SWE at the SNOTEL stations in Figure **??**a to the closest gridpoint from each WRF simulation. In all simulations, the seasonal peak in SWE is one to two months earlier than the maximum seasonal peak from the SNOTEL stations, indicating that the snow pack accumulation phase is too short and snowmelt begins generally too early in the year. The seasonal cycle is improved from NAC5 to NAC6 and C404, with a notable elongation of the maximum SWE at all stations (Figure 10b), and in the HUC-8 watershed regions focused upon in Figure 10c-e. This early peak in SWE is consistent across the diverse watershed regions in the western US. (He et al., 2021) showed that early season melt events accelerate snowmelt processes in WRF and Noah MP simulations of the western US, likely due to poorly-represented snow albedo processes, excessive downwards surface shortwave radiation, and strong surface winds that enhance surface heat exchange.

3.4 Extreme events

In the following analysis, we compare the three simulations using the “perfect model framework," treating the results from C404 as the goal-post to compare the efficacy of NAC6 and NAC5. As all datasets use spectral nudging, the large-scale circulation is quite similar between the datasets, and many weather events that are resolved by ERA5 are also resolved and simulated in these three simulations. This allows us to compare case studies and climatologies of observed extreme events to see how they were simulated by WRF in different dynamically downscaled configurations.

Figure 10 compares precipitation extremes by displaying histograms of the maximum hourly precipitation rate of each month across land surface gridpoints over the CONUS domain (130-60°W and 30-50°N). In any precipitation dataset or simulation, the frequency and intensity of extreme precipitation rates are dependent on the spatial resolution, with precipitation intensity decreasing as gridpoint area becomes larger (Chen and Dai, 2018). While spatially integrating datasets or simulations with

https://doi.org/10.5194/egusphere-2026-1638
Preprint. Discussion started: 11 May 2026

different horizontal resolution may provide more equitable precipitation rates, it is critically important to capture localized extreme rates too.

The C404 dataset simulates extreme precipitation rates that closely match station-based observational estimates (Rasmussen et al., 2023). Figure 10 shows that the probability density of extreme precipitation rates in NAC6 is very similar to C404, even without resolved convection. Precipitation rates exceeding 175 mm/hour are not produced in the 12 km NAC6, but the overall distribution of extreme rainfall events is a marked improvement over NAC5.

The following analysis examines processes historically difficult to simulate at coarser model resolutions, including a case study and climatology of tropical cyclone (TC) characteristics and a case study of a severe summertime convective storm. Hurricane Ivan is chosen as the TC case study because it was a strong TC within the temporal and spatial range of all datasets. Ivan made landfall as a Category 3 hurricane in Orange Beach, Alabama on September 16, 2004, producing a record-breaking tornado outbreak and up to 43 cm of rainfall with widespread flooding (Steward, 2004). While these simulations cannot represent the tornado outbreak, we evaluate storm intensity and impact metrics: minimum surface pressure, maximum precipitation rate, and maximum wind speed within a 150 km radius of the storm center (the gridpoint with lowest surface pressure).

Figure 11a-c shows the downward solar flux at the surface for the hurricane in each simulation. C404 clearly resolves the inner eye and spiral rainbands, with a notably symmetric pre-landfall structure indicating low wind shear, closely resembling observed Hurricane Ivan at this time (2004-09-15 18:00 UTC) (National Weather Service, Mobile/Pensacola Weather Forecast Office, 2024). NAC6 also resolves important storm characteristics, including a well-defined eye, coarse spiral banding, and symmetric structure (Figure 11b). At 25 km, NAC5 still resolves a central eye but fails to depict realistic spiral banding or storm symmetry (Figure 11c).

NAC6 also reliably produces metrics describing storm intensity and potential impacts (Figure 11d-f). Both C404 and NAC6 show very similar evolutions of minimum surface pressure, maximum precipitation rate, and maximum wind speed while the TC was in the Gulf of Mexico (September 14 through 17). TC metrics from NAC5 are comparably very weak.

We extend this analysis into a climatology by evaluating the same metrics—minium pressure, maximum precipitation rate, and maximum 10-meter wind speed—for every TC that tracked into the Gulf of Mexico within 20-40°N and 105-75°W, and was labeled a hurricane by the National Hurricane Center. We use the IBTRACS TC data for an initial guess at the storm location (the actual storm center in each WRF simulation is obtained by finding the minimum surface pressure within 50 km of the IBTRACS storm location) and for the TC category as defined by the US National Hurricane Center.

Violin and box plots of these metrics are shown for the three simulations in Figure 12. For all three intensity metrics, the C404 and NAC6 runs have similar distributions associated with TCs, with the strongest similarly shown for minimum pressure (Figure 12a) and maximum precipitation (Figure 12b). The wind speed distributions do clearly decrease with the resolution (Figure 12c), but NAC6 still performs well compared to C404. These results suggest that the NAC6 dataset is suitable for analyzing larger-scale statistics and impacts of tropical cyclones. Research focused on TC dynamics and storm structure (for example, eyewall updrafts and mesovortices) requires a much higher resolution than even 4 km (Liu et al., 2021).

Convectively generated mid-latitude storms pose substantial threats to human life and cause significant economic damage each year (Ashley and Mote, 2005; Wade et al., 2025), especially in central North America. The most impactful are often

https://doi.org/10.5194/egusphere-2026-1638
Preprint. Discussion started: 11 May 2026

mesoscale convective systems (MCSs), in which localized convection organizes into larger propagating complexes of intense thunderstorm activity, sometimes producing powerful windstorms or derechos.

On July 22, 2003, a powerful MCS known as the "Mid-South Derecho" propagated from Arkansas through Northern Alabama with wind gusts exceeding 40 $m\,s^{-1}$ (McNeil et al., 2003). We compare the severe storm environment across the three runs using 850 hPa horizontal moisture flux ($|\mathbf{Q}| = \sqrt{(qu)^2 + (qv)^2}$) into the Midwest on July 22, 2003 (Figure 13). Moisture flux at this level indicates increased atmospheric instability and potential for heavier precipitation (Gimeno-Sotelo and Gimeno, 2023; Barlow et al., 2019). As all datasets use spectral nudging of circulation fields, the large-scale circulation (500 hPa) is similar across simulations, but notable differences emerge in the moisture flux fields, which are not nudged in C404 and NAC6. We do not expect parameterized convection to adequately simulate an MCS, but highlight differences in the resolved storm environment across simulations.

Figure 13 shows substantially different mesoscale storm structures in the three WRF runs. All datasets produce an elongated longitudinal band of enhanced moisture flux aligned with low-level winds, but smaller-scale convective features are only present in C404, visible as localized areas ($<$ 20 km) of enhanced moisture flux, particularly in the northeast quadrant of Figure 13a. Both NAC6 and NAC5 resolve a more contiguous moisture flux band lacking these smaller-scale convective features (Figure 13b-c).

Figure 13d-e highlights the importance of convection-permitting scales for representing distributions of moisture flux convergence (MFC; Equation 2; Figure 13d) and temperature advection (Equation 3; Figure 13e), two metrics associated with intense localized instability and extreme precipitation rates (spatial plots in Figure S5). All simulations exhibit distributions centered near zero with similar overall structure, but both CORDEX simulations have substantially narrower distributions than the convection-resolving dataset, with far fewer high-magnitude convergence and advection events. While NAC6 resolves slightly larger magnitudes than NAC5, this difference is modest compared to the contrast with the 4 km simulation (Figure 13), indicating that resolved convection is needed to capture the localized magnitudes of atmospheric processes in severe convective storms.

$$MFC = -\int_{850_{hPa}}^{700_{hPa}} \left(\frac{\partial(qu)}{\partial x} + \frac{\partial(qv)}{\partial y} \right) dp \tag{2}$$

$$-\mathbf{V} \cdot \nabla T = -\left(u\frac{\partial T}{\partial x} + v\frac{\partial T}{\partial y} \right) \tag{3}$$

4 Conclusions

Our evaluation demonstrates notable improvements in the NAC6 configuration across nearly all metrics examined over NAC5. This 12-km ERA5-driven simulation exhibits reduced biases in temperature, precipitation, and snow, enhanced representation of diurnal processes, and improved simulation of extreme events compared to the previous-generation NAC5 simulation.

https://doi.org/10.5194/egusphere-2026-1638
Preprint. Discussion started: 11 May 2026

Particularly encouraging is the performance of extreme precipitation rates, which compare favorably with the convection-permitting C404 dataset. These results support NAC6 as a robust framework for investigating long-term changes in extreme precipitation and regional climate variability. Additionally, both our case-study analysis and climatological metrics of tropical cyclones simulated by NAC6 show promising skill, indicating the configuration's ability to represent key weather systems at convection-parameterized scales.

Relative to NAC6, the convection-permitting C404 simulation shows clear advantages in specific areas: reduced warm biases in daily minimum temperatures across the western US, more realistic diurnal temperature ranges, and superior representation of diurnal precipitation phasing, including the eastward propagation of convective events from the Rocky Mountains into the Great Plains and Midwest. C404 also shows modestly reduced SWE biases at high elevations. However, for precipitation, the comparison is more nuanced: NAC6 exhibits a less severe dry bias in parts of the western US, and relative skill varies by region and season with no uniformly superior dataset. For resolved-scale climate characteristics such as mean temperature and precipitation biases, extreme precipitation rates, and tropical cyclone intensity, NAC6 demonstrates performance broadly consistent with C404 while offering the computational efficiency required for ensemble-based uncertainty quantification.

Our case-study analysis of a severe convective storm environment highlights the clearest resolution gap: the sharp temperature and moisture gradients that produce localized extremes during convective storms were only realistically simulated in C404, rendering both NAC6 and NAC5 less suitable for studies focused specifically on convective storm dynamics. Nevertheless, there is substantial value in simulations at 12 km resolution, particularly given computational constraints.

At the time of writing, fully convection-permitting long-term climate ensembles that sample structural and emissions-scenario uncertainty (Qian et al., 2016) remain computationally prohibitive, especially over a large domain such as North America. Our results demonstrate that 12-km simulations provide substantial and scientifically robust information about weather and climate processes while enabling ensemble breadth. In this context, the 12-km CORDEX simulations will serve as a practical and defensible "workhorse" for dynamical downscaling efforts aimed at quantifying multiple sources of climate uncertainty. Continued reduction of climatological bias remains an important objective, but the demonstrated performance of NAC6 supports its use for ensemble-based downscaling and climate studies (Paquin et al., 2025; Rahimi et al., 2022).

This evaluation run represents one component of the planned NA-CORDEX-CMIP6 simulation suite. At the time of writing, simulations downscaling multiple CMIP6 ESMs with WRF are well underway, and their outputs will be made publicly available through the NSF National Center for Atmospheric Research's Global Geoscience Data Exchange (NCAR GDEX). These ensemble simulations will enable more comprehensive assessments of climate change impacts across North America and provide crucial information for regional adaptation and decision-making.

Code and data availability. The WRF model version 4.6.1 used in this study is open source and released under a public domain license. The exact source code is archived on Zenodo at https://doi.org/10.5281/zenodo.19010235 (Skamarock et al., 2019). The ERA5 reanalysis model-level data used to force the NAC6 and C404 simulations are available from the NSF NCAR Geoscience Data Exchange (GDEX) (https://doi.org/10.5065/XV5R-5344) (Hersbach et al., 2020). ERA5-Land data used as a reference for climatological biases are also avail-

https://doi.org/10.5194/egusphere-2026-1638
Preprint. Discussion started: 11 May 2026

able from GDEX (https://doi.org/10.5065/SNVE-T250) (Balsamo et al., 2015). GPM IMERG V07B precipitation data used for diurnal cycle evaluation are available from GDEX (https://doi.org/10.5065/KRNV-Y644) (Huffman et al., 2023). The University of Arizona 4 km gridded SWE dataset is available from the NASA National Snow and Ice Data Center DAAC (https://doi.org/10.5067/0GGPB220EX6A) (Broxton et al., 2019). SNOTEL station data are maintained by the USDA Natural Resources Conservation Service (https://www.nrcs.usda.gov/wps/portal/wcc/home/snowData/); the aggregated datafile used in this study is archived on Zenodo (https://doi.org/10.5281/zenodo.19010235) (Stuivenvolt-Allen et al., 2026). The IBTrACS tropical cyclone best track data are available from NOAA NCEI (https://doi.org/10.25921/82ty-9e16) (Gahtan et al., 2024). The CONUS404 simulation output is available from GDEX (https://doi.org/10.5065/ZYY0-Y036) (Rasmussen et al., 2023). The NA-CORDEX-CMIP5 dataset is available from GDEX (https://doi.org/10.5065/D6SJ1JCH) (Mearns et al., 2017). Data and Python scripts needed to reproduce the analysis of the NAC6 simulation and derived analysis products supporting all figures in this study are archived on Zenodo along with our customized WRF namelist and model source code (https://doi.org/10.5281/zenodo.19010235). The NAC6 simulation output will be archived on NCAR GDEX (DOI forthcoming prior to final publication). All datasets are available under open-access licenses unless otherwise noted.

Author contributions. JSA, TE, and SR configured the WRF model. JSA and TE performed the simulations. JSA, TE, RM, MB, SR, and HIC contributed to the selection of model physics and configuration options. All authors contributed to the study methodology. JSA conducted all analyses, developed the analysis code, and wrote the original draft. TE, RM, MB, SR, HIC, and SM reviewed and edited the manuscript. RM acquired funding. SR provided computational resources.

Competing interests. The authors have the following competing interests: Jacob Stuivenvolt-Allen, Rachel McCrary, Seth McGinnis, Stefan Rahimi, and Melissa Bukovsky collaborate and work with Dr. Paul Ullrich, an editor of GMD. Other than that, we have not competing interests in the review process.

Acknowledgements. This material is based upon work supported by the NSF National Center for Atmospheric Research, which is a major facility sponsored by the U.S. National Science Foundation under Cooperative Agreement No. 1852977. We acknowledge support for high-performance computing using Derecho provided by NCAR's Computational and Information Systems Laboratory. Additionally, the setup and configuration of WRF was aided by the expertise and support of Cenlin He, Jared Lee, and Zhe Zhang at NSF NCAR.

https://doi.org/10.5194/egusphere-2026-1638
Preprint. Discussion started: 11 May 2026

References

Abolafia-Rosenzweig, R., He, C., Chen, F., and Barlage, M.: Evaluating and enhancing snow compaction process in the Noah-MP land surface model, Journal of Advances in Modeling Earth Systems, 16, e2023MS003 869, 2024.

Ashley, W. S. and Mote, T. L.: Derecho hazards in the United States, Bulletin of the American Meteorological Society, 86, 1577–1592, 2005.

Bae, S. Y., Hong, S.-Y., and Lim, K.-S. S.: Coupling WRF double-moment 6-class microphysics schemes to RRTMG radiation scheme in weather research forecasting model, Advances in Meteorology, 2016, 5070 154, 2016.

Balsamo, G., Albergel, C., Beljaars, A., Boussetta, S., Brun, E., Cloke, H., Dee, D., Dutra, E., Muñoz-Sabater, J., Pappenberger, F., et al.: ERA-Interim/Land: a global land surface reanalysis data set, Hydrology and Earth System Sciences, 19, 389–407, 2015.

Barlage, M., Chen, F., Rasmussen, R., Zhang, Z., and Miguez-Macho, G.: The importance of scale-dependent groundwater processes in land-atmosphere interactions over the central United States, Geophysical Research Letters, 48, e2020GL092 171, 2021.

Barlow, M., Gutowski Jr, W. J., Gyakum, J. R., Katz, R. W., Lim, Y.-K., Schumacher, R. S., Wehner, M. F., Agel, L., Bosilovich, M., Collow, A., et al.: North American extreme precipitation events and related large-scale meteorological patterns: a review of statistical methods, dynamics, modeling, and trends, Climate Dynamics, 53, 6835–6875, 2019.

Berg, L. K., Gustafson Jr, W. I., Kassianov, E. I., and Deng, L.: Evaluation of a modified scheme for shallow convection: Implementation of CuP and case studies, Monthly weather review, 141, 134–147, 2013.

Boos, W. R. and Pascale, S.: Mechanical forcing of the North American monsoon by orography, Nature, 599, 611–615, 2021.

Broxton, P., Zeng, X., and Dawson, N.: Daily 4 km Gridded SWE and Snow Depth from Assimilated In-Situ and Modeled Data over the Conterminous US, Version 1, https://doi.org/10.5067/0GGPB220EX6A, 2019.

Bukovsky, M. S. and Karoly, D. J.: Precipitation simulations using WRF as a nested regional climate model, Journal of applied Meteorology and Climatology, 48, 2152–2159, 2009.

Bukovsky, M. S. and Karoly, D. J.: A regional modeling study of climate change impacts on warm-season precipitation in the central United States, Journal of Climate, 24, 1985–2002, 2011.

Bukovsky, M. S. and Mearns, L. O.: Regional climate change projections from NA-CORDEX and their relation to climate sensitivity, Climatic Change, 162, 645–665, 2020.

Chen, D. and Dai, A.: Dependence of estimated precipitation frequency and intensity on data resolution, Climate dynamics, 50, 3625–3647, 2018.

Dai, A.: The diurnal cycle from observations and ERA5 in precipitation, clouds, boundary layer height, buoyancy, and surface fluxes, Climate Dynamics, 62, 5879–5908, 2024.

Diez-Sierra, J., Iturbide, M., Gutiérrez, J. M., Fernández, J., Milovac, J., Cofiño, A. S., Cimadevilla, E., Nikulin, G., Levavasseur, G., Kjellström, E., Bülow, K., Horányi, A., Brookshaw, A., García-Díez, M., Pérez, A., Baño-Medina, J., Ahrens, B., Alias, A., Ashfaq, M., Bukovsky, M., Buonomo, E., Cabos, W. D., Caluwaerts, S., Chou, S. C., Christensen, O. B., Ciarlò, J. M., Coppola, E., Corre, L., Demory, M.-E., Djurdjevic, V., Evans, J. P., Fealy, R., Feldmann, H., Jacob, D., Jayanarayanan, S., Katzfey, J., Keuler, K., Kittel, C., Kurnaz, M. L., Laprise, R., Lionello, P., McGinnis, S., Mercogliano, P., Nabat, P., Önol, B., Ozturk, T., Panitz, H.-J., Paquin, D., Pieczka, I., Raffaele, F., Remedio, A. R., Scinocca, J., Sevault, F., Somot, S., Steger, C., Tangang, F., Teichmann, C., Termonia, P., Thatcher, M., Torma, C., van Meijgaard, E., Vautard, R., Warrach-Sagi, K., Winger, K., and Zittis, G.: CORDEX model component description, https://doi.org/10.5281/zenodo.6553526, 2022.

https://doi.org/10.5194/egusphere-2026-1638
Preprint. Discussion started: 11 May 2026

Dirmeyer, P. A., Cash, B. A., Kinter III, J. L., Jung, T., Marx, L., Satoh, M., Stan, C., Tomita, H., Towers, P., Wedi, N., et al.: Simulating the diurnal cycle of rainfall in global climate models: Resolution versus parameterization, Climate dynamics, 39, 399–418, 2012.

European Centre for Medium-Range Weather Forecasts: ERA5 Reanalysis Model Level Data, https://doi.org/10.5065/XV5R-5344, 2022.

Gahtan, J., Knapp, K. R., Schreck, C. J. I., Diamond, H. J., Kossin, J. P., and Kruk, M. C.: International Best Track Archive for Climate Stewardship (IBTrACS) Project, Version 4.01, https://doi.org/10.25921/82ty-9e16, [indicate subset used]; accessed [access date], 2024.

Geerts, B., Parsons, D., Ziegler, C. L., Weckwerth, T. M., Biggerstaff, M. I., Clark, R. D., Coniglio, M. C., Demoz, B. B., Ferrare, R. A., Gallus Jr, W. A., et al.: The 2015 plains elevated convection at night field project, Bulletin of the American Meteorological Society, 98, 767–786, 2017.

Gensini, V. A., Haberlie, A. M., and Ashley, W. S.: Convection-permitting simulations of historical and possible future climate over the contiguous United States, Climate Dynamics, 60, 109–126, 2023.

Gimeno-Sotelo, L. and Gimeno, L.: Where does the link between atmospheric moisture transport and extreme precipitation matter?, Weather and Climate Extremes, 39, 100 536, 2023.

Giorgi, F. and Gutowski Jr, W. J.: Regional dynamical downscaling and the CORDEX initiative, Annual review of environment and resources, 40, 467–490, 2015.

Gutowski Jr, W. J., Ullrich, P. A., Hall, A., Leung, L. R., O'Brien, T. A., Patricola-DiRosario, C., Arritt, R. W., Bukovsky, M. S., Calvin, K. V., Feng, Z., et al.: The ongoing need for high-resolution regional climate models: Process understanding and stakeholder information, Bulletin of the American Meteorological Society, 101, E664–E683, 2020.

He, C., Chen, F., Abolafia-Rosenzweig, R., Ikeda, K., Liu, C., and Rasmussen, R.: What causes the unobserved early-spring snowpack ablation in convection-permitting WRF modeling over Utah Mountains?, Journal of Geophysical Research: Atmospheres, 126, e2021JD035 284, 2021.

He, C., Valayamkunnath, P., Barlage, M., Chen, F., Gochis, D., Cabell, R., Schneider, T., Rasmussen, R., Niu, G.-Y., Yang, Z.-L., et al.: Modernizing the open-source community Noah with multi-parameterization options (Noah-MP) land surface model (version 5.0) with enhanced modularity, interoperability, and applicability, Geoscientific Model Development, 16, 5131–5151, 2023.

Hersbach, H., Bell, B., Berrisford, P., Hirahara, S., Horányi, A., Muñoz-Sabater, J., Nicolas, J., Peubey, C., Radu, R., Schepers, D., et al.: The ERA5 global reanalysis, Quarterly journal of the royal meteorological society, 146, 1999–2049, 2020.

Holt, T. R., Niyogi, D., Chen, F., Manning, K., LeMone, M. A., and Qureshi, A.: Effect of land–atmosphere interactions on the IHOP 24–25 May 2002 convection case, Monthly Weather Review, 134, 113–133, 2006.

Hong, S.-Y., Dudhia, J., and Chen, S.-H.: A revised approach to ice microphysical processes for the bulk parameterization of clouds and precipitation, Monthly weather review, 132, 103–120, 2004.

Hosseini-Moghari, S.-M. and Tang, Q.: Can IMERG data capture the scaling of precipitation extremes with temperature at different time scales?, Geophysical Research Letters, 49, e2021GL096 392, 2022.

Huffman, G. J., Bolvin, D. T., Joyce, R., Kelley, O. A., Nelkin, E. J., Portier, A., Stocker, E. F., Tan, J., Watters, D. C., and West, B. J.: IMERG V07 release notes, Goddard Space Flight Center: Greenbelt, MD, USA, 1140, 2023.

Iacono, M. J., Delamere, J. S., Mlawer, E. J., Shephard, M. W., Clough, S. A., and Collins, W. D.: Radiative forcing by long-lived greenhouse gases: Calculations with the AER radiative transfer models, Journal of Geophysical Research: Atmospheres, 113, 2008.

Ikeda, K., Rasmussen, R., Liu, C., Gochis, D., Yates, D., Chen, F., Tewari, M., Barlage, M., Dudhia, J., Miller, K., et al.: Simulation of seasonal snowfall over Colorado, Atmospheric Research, 97, 462–477, 2010.

https://doi.org/10.5194/egusphere-2026-1638
Preprint. Discussion started: 11 May 2026

Jach, L., Schwitalla, T., Branch, O., Warrach-Sagi, K., and Wulfmeyer, V.: Sensitivity of land–atmosphere coupling strength to changing atmospheric temperature and moisture over Europe, Earth System Dynamics, 13, 109–132, 2022.

Kunkel, K. E., Easterling, D. R., Kristovich, D. A., Gleason, B., Stoecker, L., and Smith, R.: Meteorological causes of the secular variations in observed extreme precipitation events for the conterminous United States, Journal of Hydrometeorology, 13, 1131–1141, 2012.

Langhans, W., Schmidli, J., and Schär, C.: Bulk convergence of cloud-resolving simulations of moist convection over complex terrain, Journal of the Atmospheric Sciences, 69, 2207–2228, 2012.

Lee, Y.-C. and Wang, Y.-C.: Evaluating diurnal rainfall signal performance from CMIP5 to CMIP6, Journal of Climate, 34, 7607–7623, 2021.

Li, J., Sorooshian, S., Higgins, W., Gao, X., Imam, B., and Hsu, K.: Influence of spatial resolution on diurnal variability during the North American monsoon, Journal of climate, 21, 3967–3988, 2008.

Li, J., Miao, C., Zhang, G., Fang, Y.-H., Shangguan, W., and Niu, G.-Y.: Global evaluation of the Noah-MP land surface model and suggestions for selecting parameterization schemes, Journal of Geophysical Research: Atmospheres, 127, e2021JD035 753, 2022.

Lin, T.-S., He, C., Abolafia-Rosenzweig, R., Chen, F., Wang, W., Barlage, M., and Gochis, D.: Improved snow albedo evolution in Noah-MP land surface model coupled with a physical snowpack radiative transfer scheme, Journal of Hydrometeorology, 26, 185–200, 2025.

Lindvall, J. and Svensson, G.: The diurnal temperature range in the CMIP5 models, Climate Dynamics, 44, 405–421, 2015.

Liu, C., Ikeda, K., Rasmussen, R., Barlage, M., Newman, A. J., Prein, A. F., Chen, F., Chen, L., Clark, M., Dai, A., et al.: Continental-scale convection-permitting modeling of the current and future climate of North America, Climate Dynamics, 49, 71–95, 2017.

Liu, Q., Wu, L., Qin, N., and Li, Y.: Storm-scale and fine-scale boundary layer structures of tropical cyclones simulated with the WRF-LES framework, Journal of Geophysical Research: Atmospheres, 126, e2021JD035 511, 2021.

Ma, N., Niu, G.-Y., Xia, Y., Cai, X., Zhang, Y., Ma, Y., and Fang, Y.: A systematic evaluation of Noah-MP in simulating land-atmosphere energy, water, and carbon exchanges over the continental United States, Journal of Geophysical Research: Atmospheres, 122, 12–245, 2017.

Mahony, C. R., Wang, T., Hamann, A., and Cannon, A. J.: A global climate model ensemble for downscaled monthly climate normals over North America, International Journal of Climatology, 42, 5871–5891, 2022.

McCrary, R., Mearns, L., Abel, M., Biner, S., and Bukovsky, M.: Projections of North American snow from NA-CORDEX and their uncertainties, with a focus on model resolution, Climatic Change, 170, 20, 2022.

McNeil, S. J., Howell, J. L., Garrett, G. R., and Valle, D. N.: The Mid South Derecho - 22 July 2003, Tech. rep., National Weather Service Forecast Office, Memphis, Tennessee, https://www.weather.gov/media/meg/research/July22_2003.pdf, 7777 Walnut Grove Road OM1, Memphis, TN, 38120, 2003.

Mearns, L., Giorgi, F., McDaniel, L., and Shields, C.: Analysis of variability and diurnal range of daily temperature in a nested regional climate model: Comparison with observations and doubled CO2 results, Climate Dynamics, 11, 193–209, 1995.

Mearns, L., McGinnis, S., Korytina, D., Arritt, R., Biner, S., Bukovsky, M., Chang, H.-I., Christensen, O., Herzmann, D., Jiao, Y., Kharin, S., Lazare, M., Nikulin, G., Qian, M., Scinocca, J., Winger, K., Castro, C., Frigon, A., Gutowski, W., and Kessenich, L.: The NA-CORDEX dataset, version 1.0, NCAR Climate Data Gateway, Boulder, CO, https://doi.org/10.5065/D6SJ1JCH, accessed: [insert date], 2017.

Mlawer, E. J., Taubman, S. J., Brown, P. D., Iacono, M. J., and Clough, S. A.: Radiative transfer for inhomogeneous atmospheres: RRTM, a validated correlated-k model for the longwave, Journal of Geophysical Research: Atmospheres, 102, 16 663–16 682, 1997.

https://doi.org/10.5194/egusphere-2026-1638
Preprint. Discussion started: 11 May 2026

Muñoz-Sabater, J., Dutra, E., Agustí-Panareda, A., Albergel, C., Arduini, G., Balsamo, G., Boussetta, S., Choulga, M., Harrigan, S., Hersbach, H., et al.: ERA5-Land: A state-of-the-art global reanalysis dataset for land applications, Earth system science data, 13, 4349–4383, 2021.

National Weather Service, Mobile/Pensacola Weather Forecast Office: Powerful Hurricane Ivan Slams the Central Gulf Coast as a Category 3 Hurricane – September 16, 2004, https://www.weather.gov/mob/ivan, last updated September 2024. Accessed March 12, 2026, 2024.

Niu, G.-Y., Yang, Z.-L., Mitchell, K. E., Chen, F., Ek, M. B., Barlage, M., Kumar, A., Manning, K., Niyogi, D., Rosero, E., et al.: The community Noah land surface model with multiparameterization options (Noah-MP): 1. Model description and evaluation with local-scale measurements, Journal of Geophysical Research: Atmospheres, 116, 2011.

Paquin, D., McCray, C. D., Gauthier, C. B., Giguère, M., Asselin, O., Bourgault, P., Labonté, M.-P., and Matte, D.: The Ouranos CRCM5-CMIP6 ensemble: A dynamically downscaled ensemble of CMIP6 simulations over North America, Scientific Data, 2025.

Qian, Y., Jackson, C., Giorgi, F., Booth, B., Duan, Q., Forest, C., Higdon, D., Hou, Z. J., and Huerta, G.: Uncertainty quantification in climate modeling and projection, Bulletin of the American Meteorological Society, 97, 821–824, 2016.

Rahimi, S., Krantz, W., Lin, Y.-H., Bass, B., Goldenson, N., Hall, A., Lebo, Z. J., and Norris, J.: Evaluation of a reanalysis-driven configuration of WRF4 over the western United States from 1980 to 2020, Journal of Geophysical Research: Atmospheres, 127, e2021JD035 699, 2022.

Rasmussen, R., Liu, C., Ikeda, K., Gochis, D., Yates, D., Chen, F., Tewari, M., Barlage, M., Dudhia, J., Yu, W., et al.: High-resolution coupled climate runoff simulations of seasonal snowfall over Colorado: a process study of current and warmer climate, Journal of Climate, 24, 3015–3048, 2011.

Rasmussen, R., Chen, F., Liu, C., Ikeda, K., Prein, A., Kim, J., Schneider, T., Dai, A., Gochis, D., Dugger, A., et al.: CONUS404: The NCAR–USGS 4-km long-term regional hydroclimate reanalysis over the CONUS, Bulletin of the American Meteorological Society, 104, E1382–E1408, 2023.

Scaff, L., Prein, A. F., Li, Y., Liu, C., Rasmussen, R., and Ikeda, K.: Simulating the convective precipitation diurnal cycle in North America's current and future climate, Climate Dynamics, 55, 369–382, 2020.

Skamarock, W. C., Klemp, J. B., Dudhia, J., Gill, D. O., Liu, Z., Berner, J., Wang, W., Powers, J. G., Duda, M. G., Barker, D. M., et al.: A description of the advanced research WRF version 4, NCAR tech. note ncar/tn-556+ str, 145, 2019.

Steward, S. R.: Hurricane Ivan, Tropical Cyclone Report AL092004, National Hurricane Center, National Oceanic and Atmospheric Administration, https://www.nhc.noaa.gov/data/tcr/AL092004_Ivan.pdf, government document, accessed 2025-01-05, 2004.

Stuivenvolt-Allen, J., Eidhammer, T., McCrary, R., Bukovsky, M., Rahimi, S., Chang, H.-I., and McGinnis, S.: The North American CORDEX-CMIP6 WRF evaluation run: comparing historical simulations from 25km to convection-permitting scales, https://doi.org/10.5281/zenodo.19010235, 2026.

Tan, J., Huffman, G. J., Bolvin, D. T., and Nelkin, E. J.: Diurnal cycle of IMERG V06 precipitation, Geophysical Research Letters, 46, 13 584–13 592, 2019.

Tewari, M., Chen, F., Wang, W., Dudhia, J., LeMone, M. A., Mitchell, K., Ek, M., Gayno, G., Wegiel, J., and Cuenca, R. H.: Implementation and verification of the unified Noah land surface model in the WRF model, in: 20th Conference on Weather Analysis and Forecasting/16th Conference on Numerical Weather Prediction, American Meteorological Society, Seattle, WA, paper 14.2a, 2004.

Thompson, G., Field, P. R., Rasmussen, R. M., and Hall, W. D.: Explicit forecasts of winter precipitation using an improved bulk microphysics scheme. Part II: Implementation of a new snow parameterization, Monthly weather review, 136, 5095–5115, 2008.

https://doi.org/10.5194/egusphere-2026-1638
Preprint. Discussion started: 11 May 2026

Thompson, G., Tewari, M., Ikeda, K., Tessendorf, S., Weeks, C., Otkin, J., and Kong, F.: Explicitly-coupled cloud physics and radiation parameterizations and subsequent evaluation in WRF high-resolution convective forecasts, Atmospheric Research, 168, 92–104, 2016.

Tiedtke, M.: A comprehensive mass flux scheme for cumulus parameterization in large-scale models, Monthly weather review, 117, 1779–1800, 1989.

Trier, S., Davis, C., and Ahijevych, D.: Environmental controls on the simulated diurnal cycle of warm-season precipitation in the continental United States, Journal of the atmospheric sciences, 67, 1066–1090, 2010.

Wade, A. R., Squitieri, B. J., and Jirak, I. L.: Synoptic Characteristics of Derechos and Other Widespread Significant Severe Wind Events, Weather and Forecasting, p. e250038, 2025.

Wang, K. and Clow, G. D.: The diurnal temperature range in CMIP6 models: climatology, variability, and evolution, Journal of Climate, 33, 8261–8279, 2020.

Zhang, C., Wang, Y., and Hamilton, K.: Improved representation of boundary layer clouds over the southeast Pacific in ARW-WRF using a modified Tiedtke cumulus parameterization scheme, Monthly Weather Review, 139, 3489–3513, 2011.

Zhang, Z., He, C., Berner, J., Jaye, A., Barlage, M., Liu, C., Dudhia, J., Huang, K., Lin, T.-S., Abolafia-Rosenzweig, R., et al.: Extending MPAS-NoahMP model capability beyond weather timescale: assessing land-atmosphere interactions for future subseasonal-to-seasonal applications, Authorea Preprints, 2025.

Zheng, Y., Alapaty, K., Herwehe, J. A., Del Genio, A. D., and Niyogi, D.: Improving high-resolution weather forecasts using the Weather Research and Forecasting (WRF) Model with an updated Kain–Fritsch scheme, Monthly Weather Review, 144, 833–860, 2016.

https://doi.org/10.5194/egusphere-2026-1638
Preprint. Discussion started: 11 May 2026

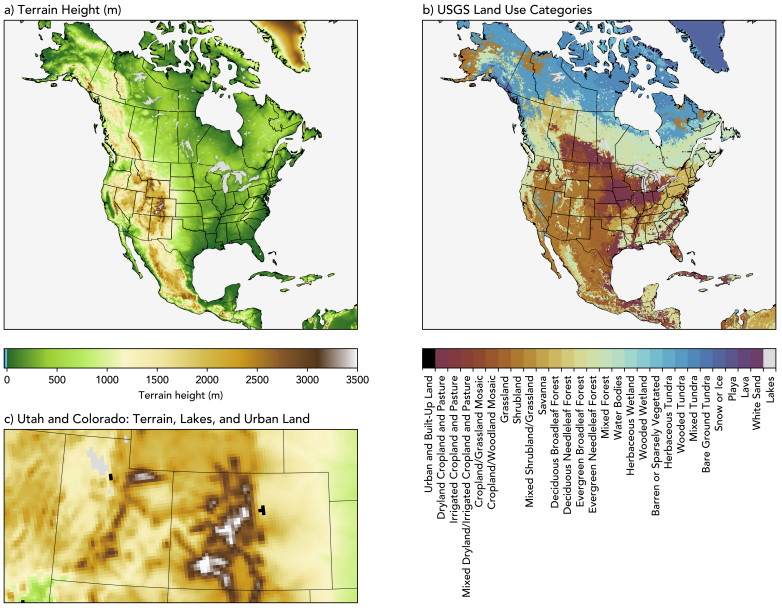

Figure 1. Terrain height (a) and USGS land-use categories with vegetation types (b) for our WRF configuration. Panel (c) shows the USGS land-use categories for a smaller domain over Utah and Colorado.

https://doi.org/10.5194/egusphere-2026-1638
Preprint. Discussion started: 11 May 2026

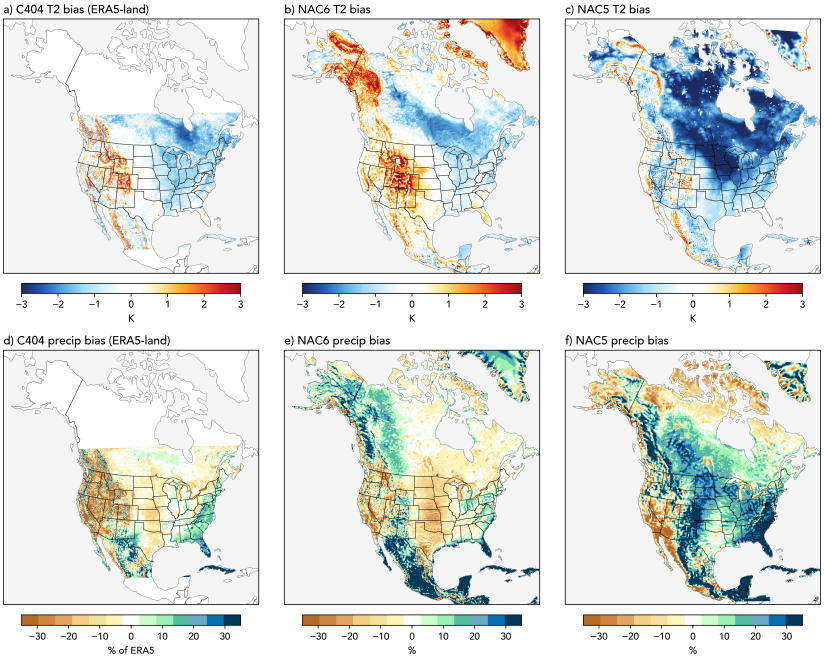

Figure 2. Climatological bias of 2-meter air temperature and precipitation for C404 (a,d), NAC6 (b,e), and NAC5 (c,f) using ERA5-Land as a reference dataset from 1980 through 2010.

https://doi.org/10.5194/egusphere-2026-1638
Preprint. Discussion started: 11 May 2026

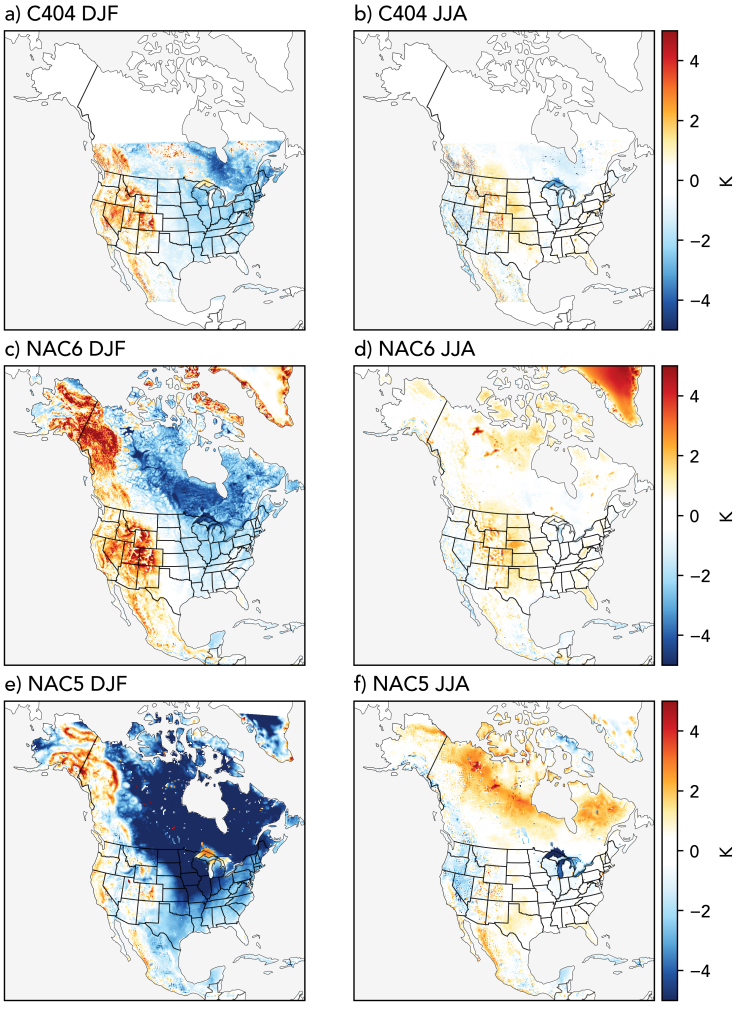

Figure 3. Winter (DJF) and Summer (JJA) climatological bias of 2-meter air temperature for C404 (a,b), NAC6 (c,d), and NAC5 (e,f) using ERA5-Land as a reference dataset.

https://doi.org/10.5194/egusphere-2026-1638
Preprint. Discussion started: 11 May 2026

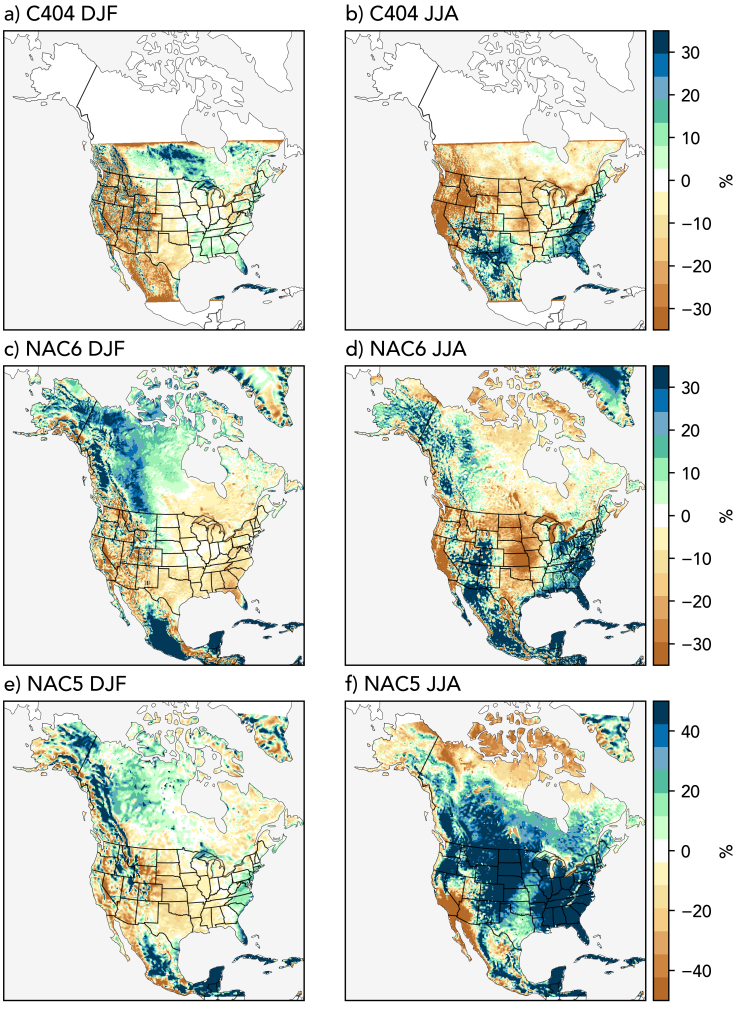

Figure 4. Same as Figure 3 but for seasonal precipitation. Biases are plotted as a percent of the climatological values from ERA5-Land.

https://doi.org/10.5194/egusphere-2026-1638
Preprint. Discussion started: 11 May 2026

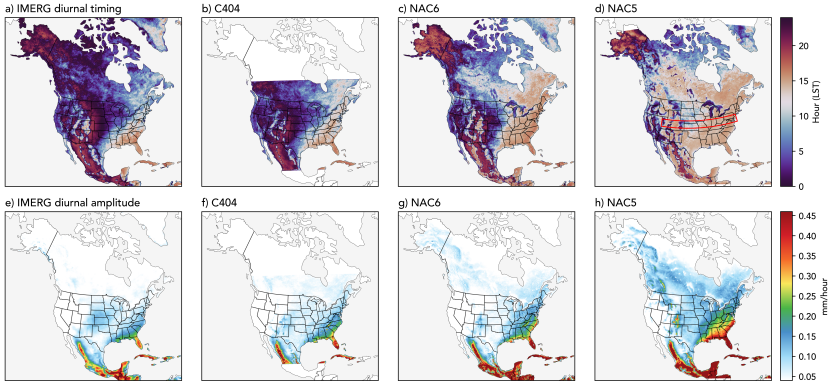

Figure 5. Diurnal precipitation peak time (top row) and magnitude (bottom row) for IMERG (a,e), C404 (b,f), NAC6 (c,g) and NAC5 (d,h) estimated using a second order harmonic fit of hourly precipitation for June, July and August. The domain for the longitude and time Hovmöller diagrams in the next figure is shown in panel (d)

https://doi.org/10.5194/egusphere-2026-1638
Preprint. Discussion started: 11 May 2026

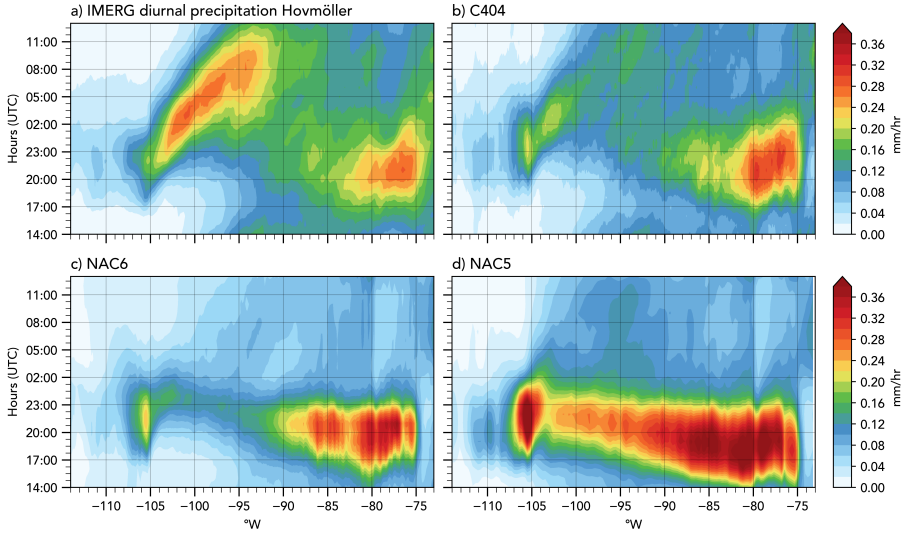

Figure 6. Longitude and time Hovmöller of hourly average precipitation for June, July, and August for 120-60°W and 38-42°N. IMERG summer means (a) are compared with C404 (b), NAC6 (c), and NAC5 (d).

https://doi.org/10.5194/egusphere-2026-1638
Preprint. Discussion started: 11 May 2026

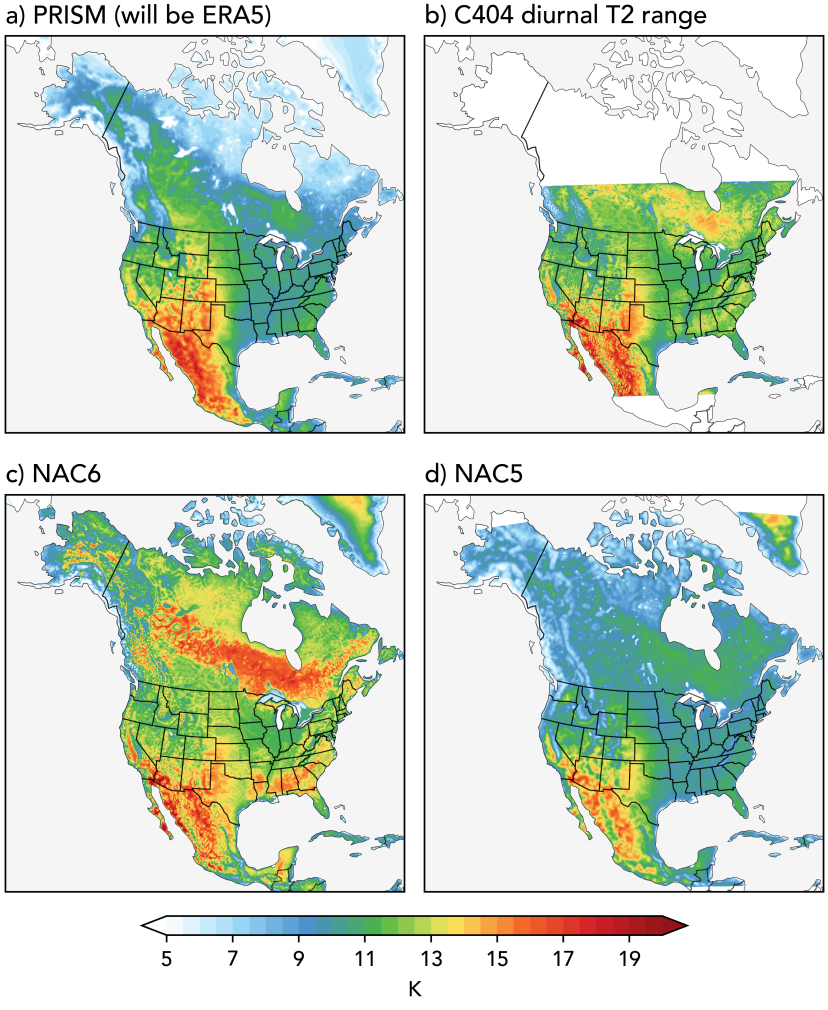

Figure 7. Average springtime (MAM) diurnal temperature range (maximum temperature minus minimum temperature) for C404 (a), NAC6 (b), NAC5 (c), and ERA5-Land (d).

https://doi.org/10.5194/egusphere-2026-1638
Preprint. Discussion started: 11 May 2026

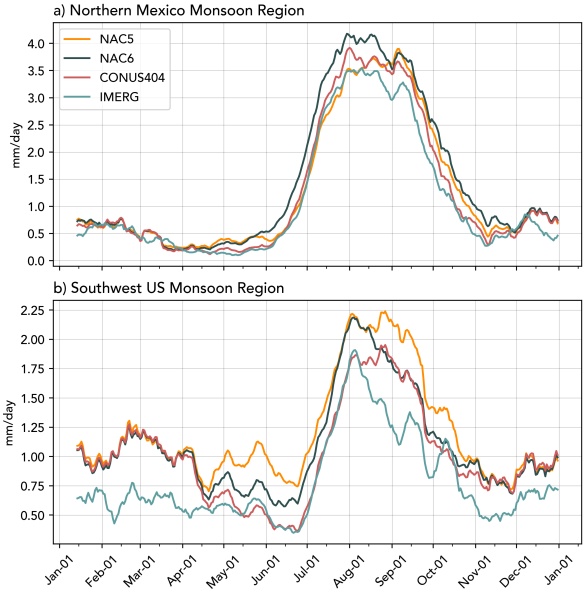

Figure 8. Daily climatological mean of precipitation for an area average in northern Mexico (115-105°W and 25-32°N) and the southern US monsoon region (115-105°W and 32-40°N). A 7-day rolling mean is applied to the data to reduce daily variability.

https://doi.org/10.5194/egusphere-2026-1638
Preprint. Discussion started: 11 May 2026

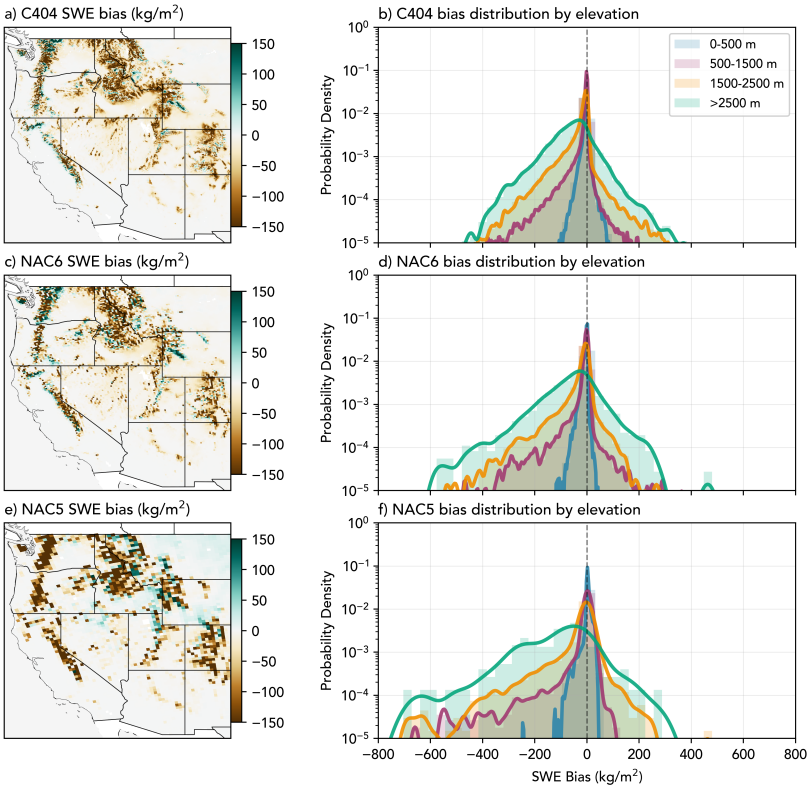

Figure 9. Gridpoint bias in SWE for late winter and early spring (JFMAM) using the University of Arizona SWE 4-km dataset as a reference (left column). The right column shows the corresponding bias distribution for elevation bands for C404 (a,b), NAC6 (c,d) and NAC5 (e,f).

https://doi.org/10.5194/egusphere-2026-1638
Preprint. Discussion started: 11 May 2026

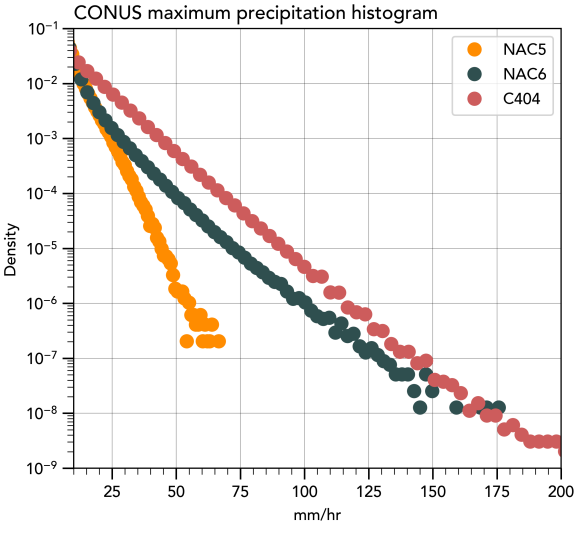

Figure 10. Histogram of monthly maximum precipitation for all land grid-points over the CONUS domain (land gridpoints spanning 130-60°W and 30-50°N).

https://doi.org/10.5194/egusphere-2026-1638
Preprint. Discussion started: 11 May 2026

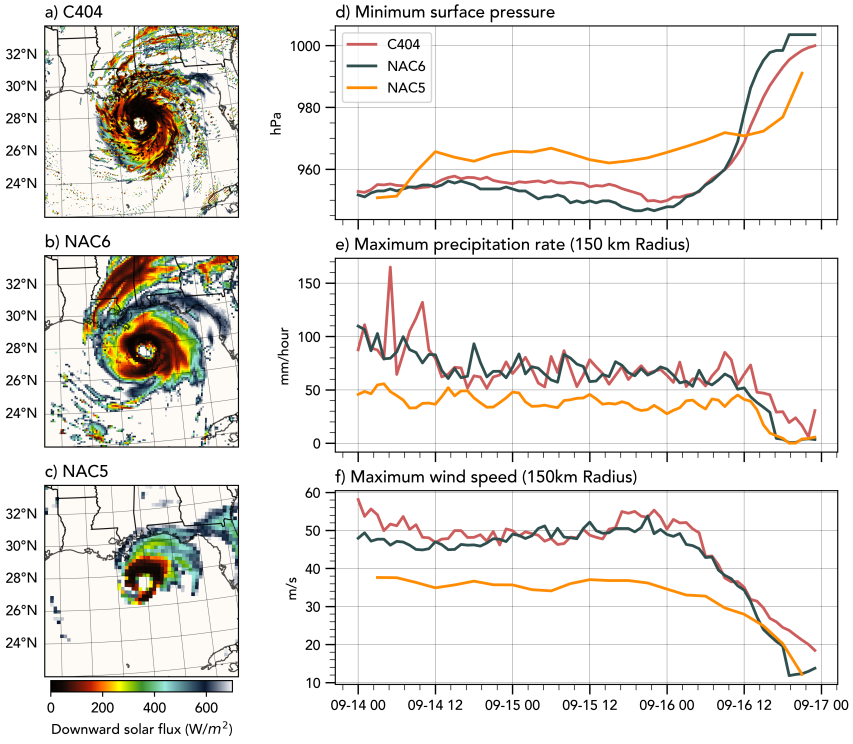

Figure 11. Shortwave radiation flux revealing cloud structure of the simulated TC on 2005-09-15 at 18:00 UTC in all three simulations (a-c). The right column shows the minimum surface pressure (d), maximum precipitation rate(e), and maximum wind speeds (f) within 150-km radius of the minimum surface pressure value.

https://doi.org/10.5194/egusphere-2026-1638
Preprint. Discussion started: 11 May 2026

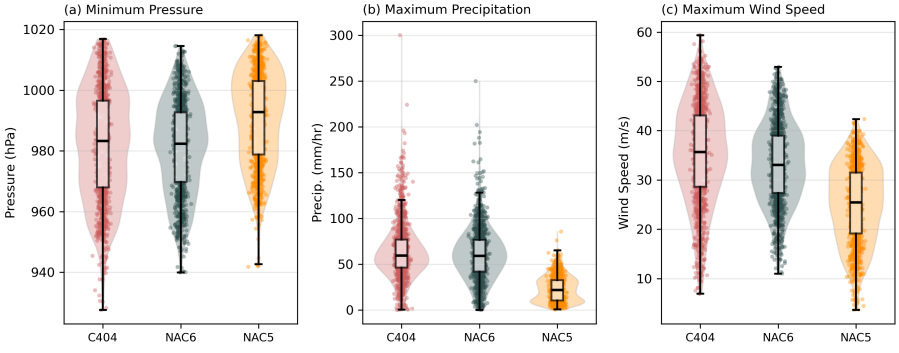

Figure 12. Violin and box plots of minimum central pressure for all TCs within the Gulf from 1980 through 2010 in each simulated dataset (a). Panels (b) and (c) similarly display the maximum precipitation and maximum wind speed within 150-km radius of the storm center.

https://doi.org/10.5194/egusphere-2026-1638
Preprint. Discussion started: 11 May 2026

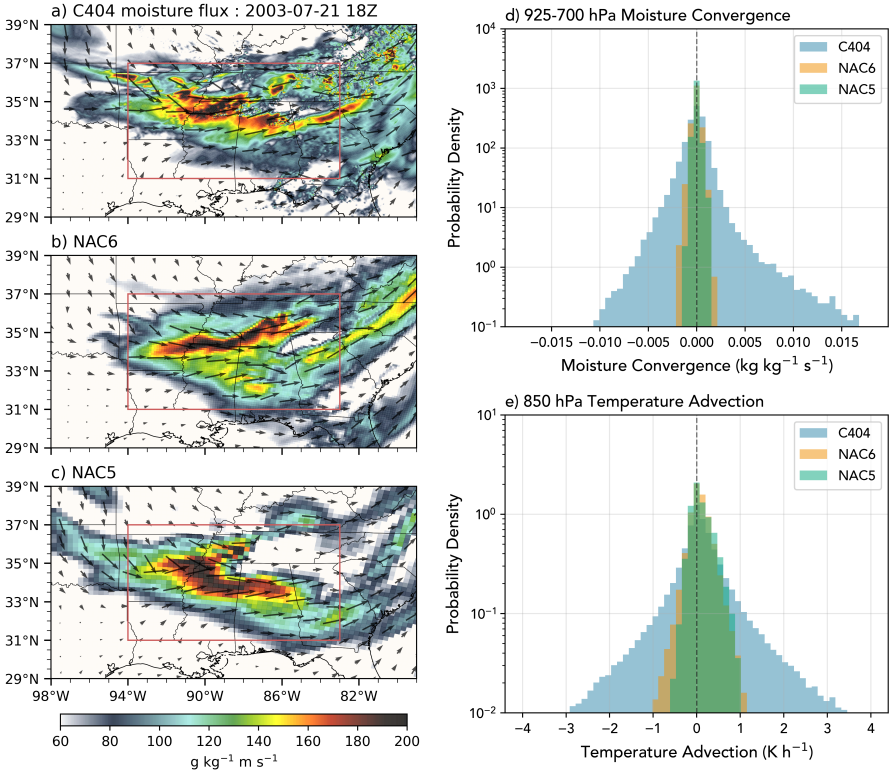

Figure 13. 750 hPa moisture flux during the "Mid-South Derecho", which translated across the southern Great Plains on July 22, 2003 (18z pictured here). Shading indicates the magnitude of moisture flux; vectors indicate the direction and magnitude. Histograms of (d) 925-700 hPa column-integrated moisture convergence and (e) 850 hPa temperature advection at 00, 06, 12, and 18Z on 2003-07-21 for each simulation over the domain shown by the red rectangle in panels a-c.